6B.4

ANALYSIS OF CONVERGENCE BOUNDARIES DURING IHOP

Roger M. Wakimoto*
National Center for Atmospheric Research
Boulder, CO 80305

Hanne V. Murphey
UCLA
Los Angeles, CA 90095

1. INTRODUCTION

There have been important advances in short-term forecasts (nowcasts) of thunderstorm initiation during the warm season. These advances are critical as illustrated by Olsen et al. (1995). They have highlighted the pronounced drop in our predictive skill during the summer months when the precipitation totals are the greatest. The improvements in our understanding of thunderstorm formation are largely attributed to the recognition that storms frequently develop near boundary layer convergence zones that are often detected by Doppler radars and satellite imagery (e.g., Purdom 1976, 1982; Wilson and Schreiber 1986; Wilson et al. 1998). Indeed, Wilson and Schreiber (1986) showed that 80% of thunderstorm initiation occurred near a surface convergence zone. It is also known, however, that the existence of a convergence boundary does not imply that convection will develop even when large convective available potential energy (CAPE) and conditionally unstable environments exist (e.g., Stensrud and Maddox 1988; Richter and Bosart 2002; Cai et al. 2006).

There have been a number of individual case studies that have examined the detail structure of convergence boundaries and their relationship to convection initiation. However, there has been no systematic attempt to perform a comprehensive analysis of a number of convergence boundaries using analogous data sets. Such an analysis would result in generalized conclusions concerning the thermodynamic and kinematic characteristics of the boundaries and the relationship to thunderstorm formation.

The current study presents airborne dual-Doppler wind syntheses and thermodynamic analysis based on soundings for six convergence boundaries during the International H_2O Project (IHOP; Weckwerth et al. 2004). The aircraft flew a box pattern around the boundaries with along-boundary legs ~100 km long. The Doppler radar data collected allowed for an assessment of both the along-frontal variability but also the mean characteristics of the convergence zone over an extended region. The flight legs also resulted in a data set with analogous spatial resolution so that direct comparisons between the case studies could be made. In addition, the kinematic and thermodynamic structure of all of these boundaries were well-documented with a series of dropsondes deployed by a jet flying at ~500 mb. The spatial and temporal resolutions of the sounding data were comparable which facilitated comparisons between the cases.

* *Corresponding author address: Roger M. Wakimoto, National Center for Atmospheric Research, P.O. Box 3000, Boulder, CO 80307; e-mail: wakimoto@ucar.edu*

2. IHOP AND THE PRIMARY DATA PLATFORMS

One of the main objectives of IHOP was to document the three-dimensional water vapor distribution in the lower troposphere in order to better understand the processes that lead to the initiation of deep convection. The field phase took place during the spring and summer of 2002 over the southern Great Plains and brought together a number of mobile platforms. These platforms were necessary in order to sample a number of convergence boundaries over an extensive geographic region. Intensive observation periods (IOPs) for six days are presented in this study. Convection initiation occurred on 24 May, 10 June, and 19 June. No storms developed in the area targeted by the research platforms (i.e., null cases) on 22 May, 11 June, and 12 June.

The data sets collected by two platforms are highlighted in this study - an airborne Doppler radar and dropsondes deployed from an aircraft. A 3-cm airborne Doppler radar (ELDORA; Electra Doppler radar) is operated by the National Center for Atmospheric Research (NCAR) and is flown on board a Naval Research Laboratory (NRL) P-3. The nominal research flight track required the P-3 to fly between 400-600 m AGL (above ground level; hereafter, all heights are AGL except where indicated) and parallel to the thin lines. The aircraft flew rectangular box-like patterns within 2-3 km on either side of the thin line. The along-boundary flight tracks were ~100 km in length.

The kinematic and thermodynamic structure in a vertical plane for the convergence boundaries was revealed by dropsondes that were deployed by a jet flying at ~500 mb. The approximate orientation of the flight track was perpendicular to the thin lines. The rapid deployment of the dropsondes from the aircraft meant the typical elapsed time between the first and last sounding was between 20-25 min.

3. SURFACE ANALYSIS AND FLIGHT TRACK

Surface analyses for the six cases are shown in Fig. 1. The IHOP field operations plan for convection initiation proposed that the intensive observing region was defined by the P-3 flight track. According, the mobile

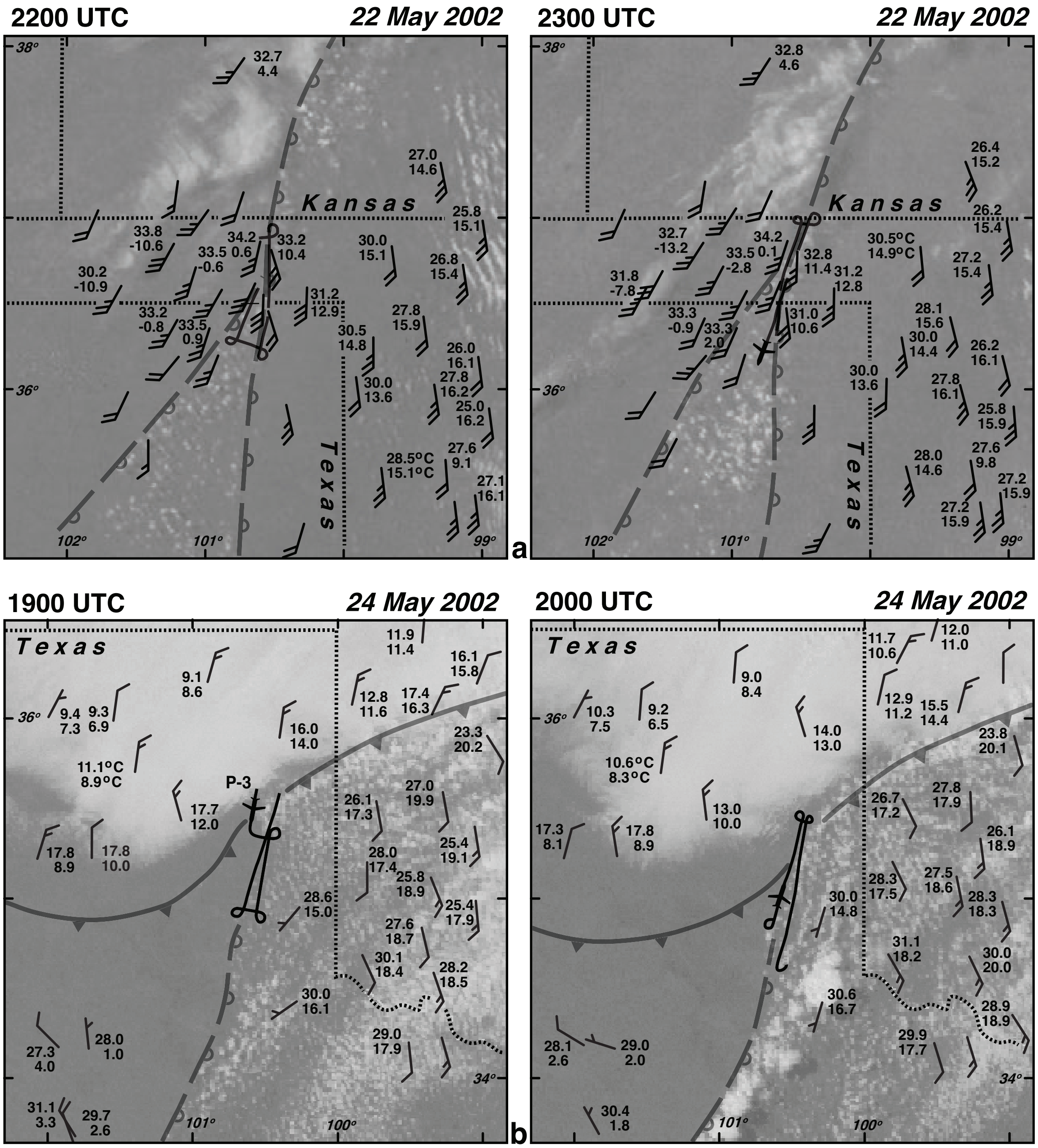

Fig. 1. Surface analysis for a) 2200 and 2300 UTC on 22 May, b) 1900 and 2000 UTC on 24 May, c) 1900 and 2000 UTC on 10 June, d) 2100 and 2200 UTC on 11 June, e) 2100 and 2200 UTC 12 June, and 2000 and 2100 UTC on 19 June superimposed onto visible satellite images. Temperature and dew-point temperature (^{o}C) are plotted. The track of the P-3 is shown by the black line. Wind vectors are plotted using the following notation: barb = 5 m s^{-1}, half barb = 2.5 m s^{-1}.

ground-based facilities and locations where dropsondes were released were concentrated near the center of the box-pattern flown by the aircraft.

A well-defined dryline that developed ahead of a cold front was the focus of the IOP on 22 May (Fig. 1a). A secondary dryline also formed to the west of the primary dryline later in day (Fig. 1a). An opportunity to examine a dryline that formed a “triple point” with a cold front where three air masses converge. ELDORA collected Doppler radar data on the dryline and the intersection of the boundary with a cold front that was at the leading edge of a Canadian air mass (Fig. 1b). The initiation of an intense squall line was documented and can be seen near the bottom half of the satellite image at 2000 (Fig. 1b). A segment of a cold front over southwest Kansas as well-sampled by the IHOP observing platforms on 10 June (Fig. 1c). An interesting aspect of this case was a nearby dryline that developed to the southeast and approximately parallel to the front as documented by Friedrich et al. (2008a and b). Conditions became

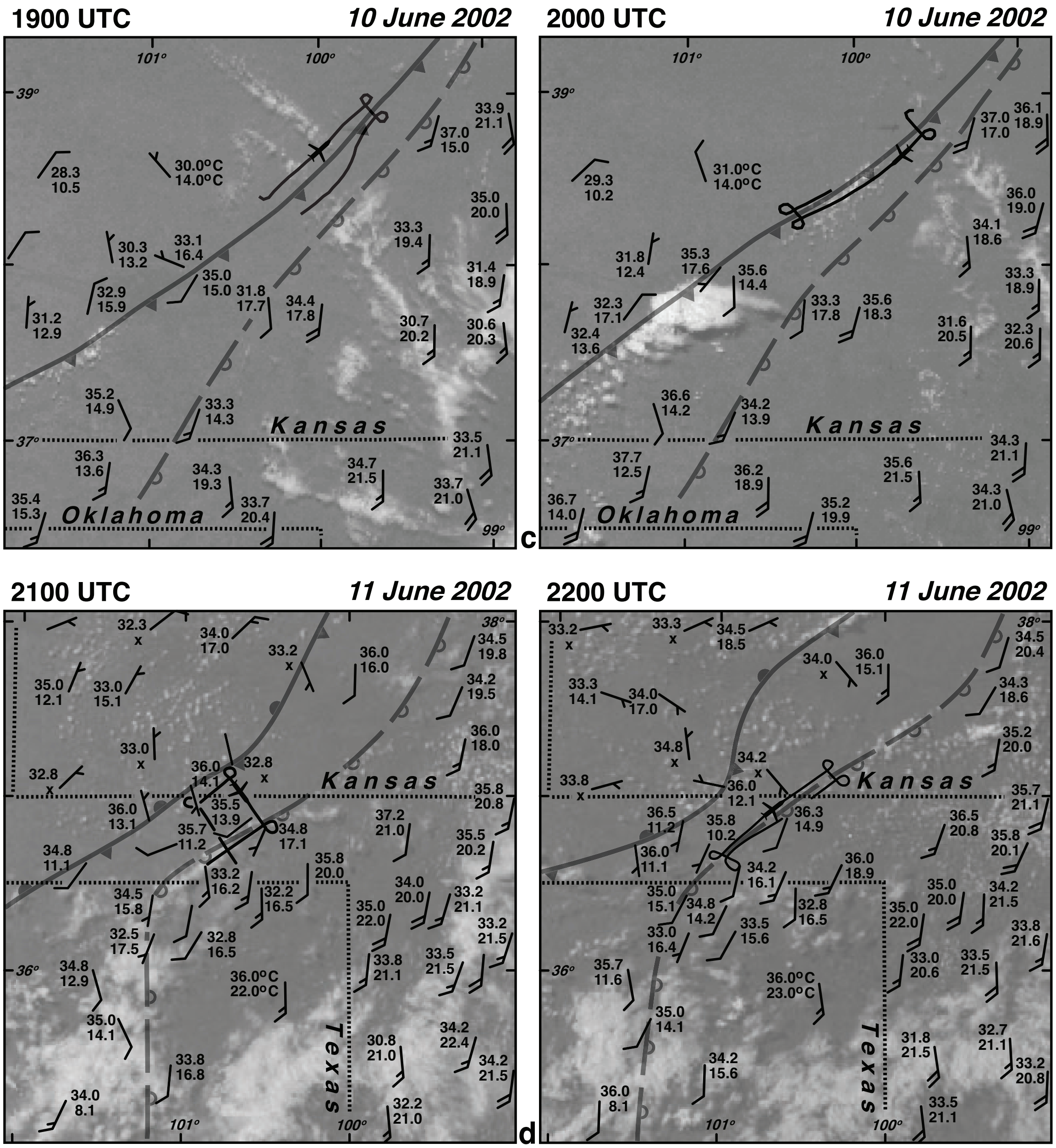

Fig. 1. Continued.

favorable for thunderstorm development as isolated cells initially formed along the southwest sector of the cold front at 2000 (Fig. 1c). The dryline on 11 June was associated with the weakest kinematic discontinuity observed during the experiment, however, there was a substantial moisture gradient across the boundary as shown by Cai et al. (2006) (Fig. 1d). No storms developed along the dryline on this day. A more complex synoptic situation formed on 12 June during IHOP (Fig. 1e). An approximate west-east oriented boundary along the Oklahoma-Kansas border was produced by an outflow from a mesoscale convective system. A dryline intersected the outflow just east of a circulation associated with mesolow in the Oklahoma panhandle. A cold front extended from the mesolow and merged with a dryline in the western Texas panhandle. Although convection initiated along the outflow boundary (Fig. 1e), it occurred at the far eastern edge of the observational area defined by the P-3 flight track (Markowski et al. 2006; Weckwerth et al. 2008). This case is classified as a null case since no convection developed along the primary region of the boundary sampled by the P-3. The final case analyzed is a dryline that developed parallel to and just east of cold front in northwest Kansas on 19 June (Fig. 1f). The first legs flown along the dryline by the P-3 occurred under clear skies. Subsequently, a strong squall line initiated along the entire boundary as shown in Fig. 1f.

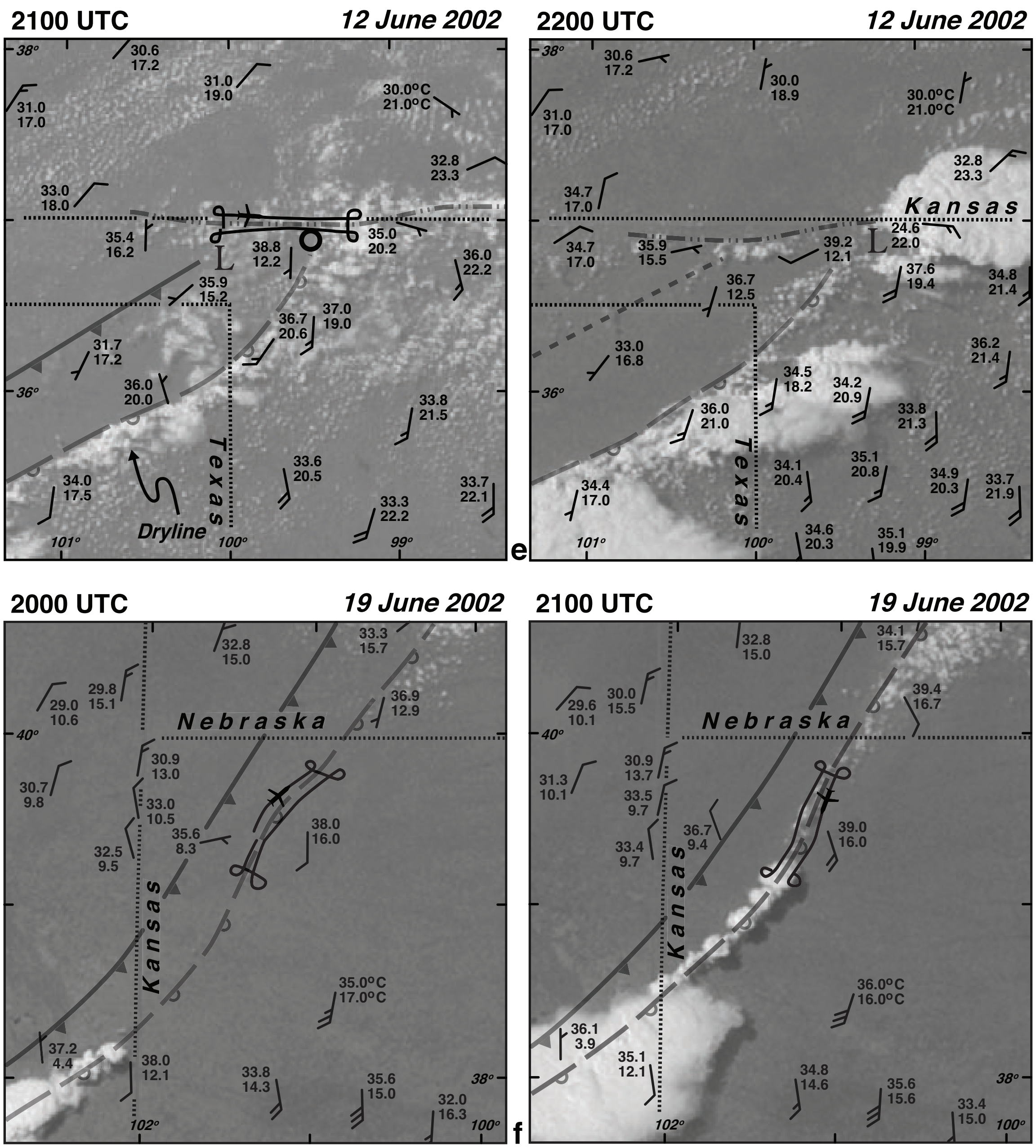

Fig. 1. Continued.

4. DUAL-DOPPLER ANALYSES

Representative examples of the dual-Doppler wind syntheses are shown in Fig. 2. The dryline on 22 May was well-sampled by ELDORA based on numerous flight legs by the P-3. Confluence can be seen in the surface analysis and the dual-Doppler wind synthesis (Fig. 2a). There is a cellular echo pattern in the thin line resolved by ELDORA and the maximum radar reflectivity is >6 dBZ. The intersection of the dryline and the cold front on 24 May results in an echo pattern that resembles an "inverted-V". The cold front/dryline intersection is easily identified in the ELDORA analysis and the aircraft collected in situ measurements at flight level near the triple point (Fig. 2b). There is pronounced cyclonic shift of the dual-Doppler winds across the dryline. The cold front and the approximate position of a dryline on 10 June is shown in Fig. 1c. The existence of the dryline was shown in a series of analyses presented by Friedrich et al. (2008a and b). The thin line accompanying the cold front was identified in the surveillance scan and was the primary boundary that the P-3 flew along (Fig. 2c). The gray lines in Fig. 2c indicated the positions of two horizontal convective rolls (HCRs). The intersections of HCRs with convergence boundaries have been hypothesized to be locations where convection may initiate. The maximum values of radar reflectivity along the thin line occur near the intersection points. Wilson et al. (1994) proposed that these areas delineate the

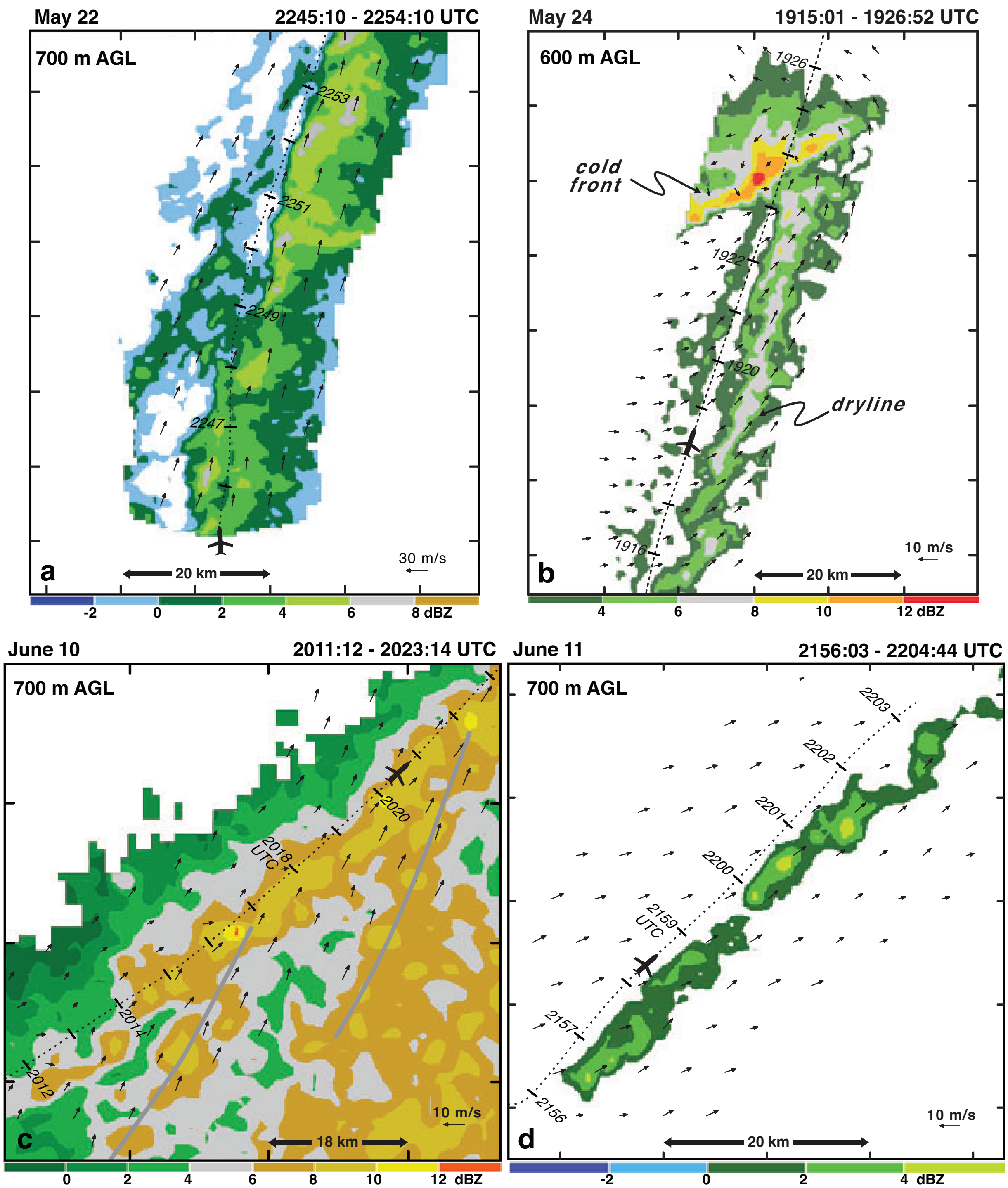

Fig. 2. Airborne dual-Doppler radar analysis for (a) 2245 - 2254 UTC on 22 May, (b) 1915 - 1926 UTC on 24 May, (c) 2011 - 2023 UTC on 10 June, (d) 2156 - 2204 UTC on 11 June, (e) 2009 - 2021 UTC 12 June, and (f) 2029 - 2042 UTC 19 June superimposed onto radar reflectivity at 700 m AGL. Flight track of the P-3 is shown by the dashed line.

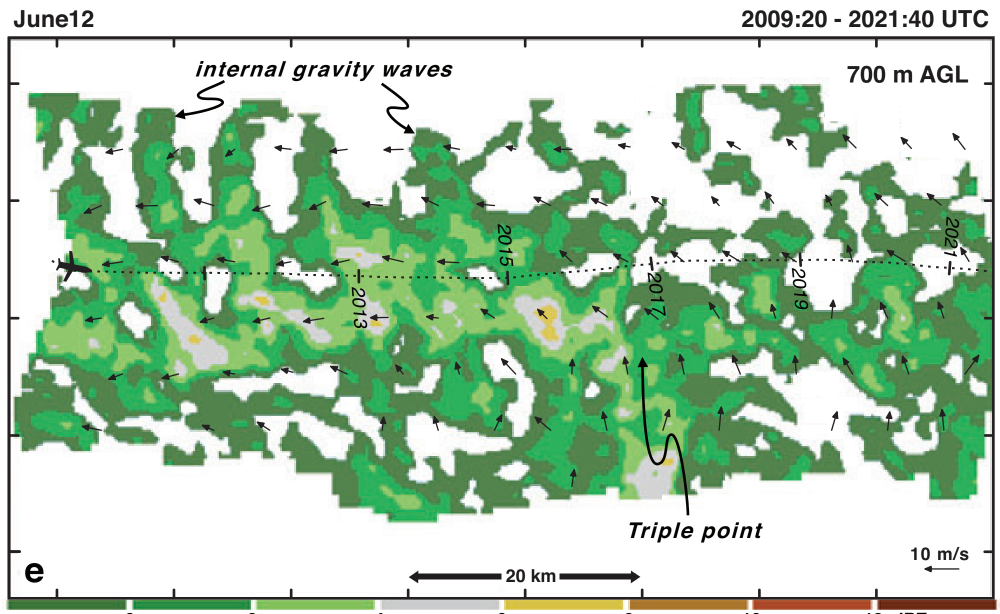

Fig. 2. Continued.

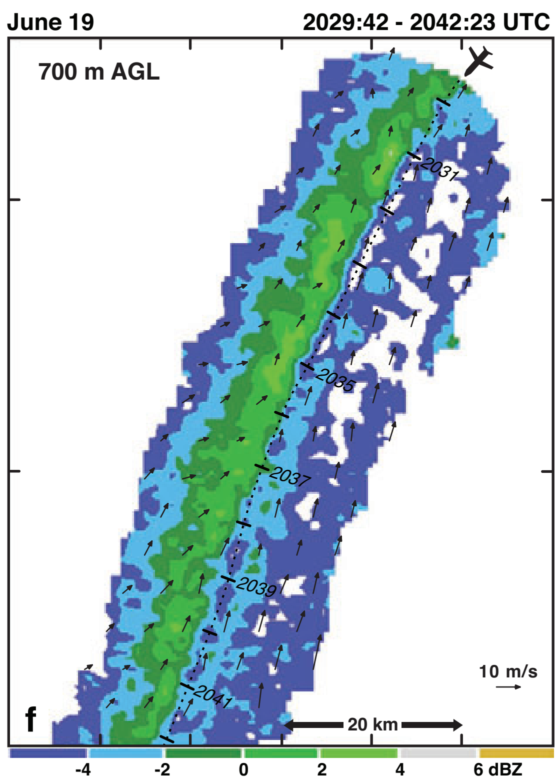

maximum surface convergence.

A dryline developed on 11 June and was associated with the weakest kinematic discontinuity observed during IHOP. The moisture contrast across the boundary, however, was substantial (Cai et al. 2006). The fine line based on ELDORA data was apparent (Fig. 2d) but not as well-defined as the other cases. The horizontal convergence and derived updrafts based on the wind syntheses (not shown) were weak and the wind shift across the dryline was not distinct (Fig. 2d). The P-3 flew along an outflow boundary and a triple point located at the intersection of the outflow boundary with a dryline on 12 June. North-south oriented banded structures in the radar reflectivity plots shown in Fig. 2e that emanate from the outflow boundary thin line have been hypothesized to be internal gravity waves (Weckwerth et al. 2008). A shift of the winds from southerly to easterly in the air masses located south and north of the outflow boundary, respectively, can be seen in Fig. 2e. The P-3 collected data on a dryline that formed parallel to and east of a cold front in northwestern Kansas on 19 June. Strong northwesterly and southerly flow in the post-frontal and pre-dryline air masses, respectively, were apparent on this day. Dry, westerly winds were apparent in the dry air between the two boundaries. Intensive observations along the dryline commenced before clouds developed on this day. Data collection continued until an intense squall line developed along dryline (Murphey et al. 2006). The radar fine line denoting the position of the dryline is clearly apparent in Figs. 2f.

The long flight legs flown by the P-3 provided an opportunity to reconstruct the mean vertical structure of the six boundaries by averaging individual vertical cross sections from the dual-Doppler wind syntheses. The averaging was effective in removing the along-line variability that existed (Fig. 3). The analyses presented in the figure reveals the wide variety of fine line and updraft characteristics for the various boundaries. Average profiles across the convergence boundaries for a number of kinematic and thermodynamic variables are shown in Fig. 4. The kinematic profiles were created by averaging the Doppler wind syntheses at 700 m for all legs flown during a single mission.

Visual inspection of Fig. 2 suggests that the widths of the fine lines, based on radar reflectivity, are variable. This is also supported by the approximate “bell-shaped distributions” presented in Fig. 4a. It is apparent in the figure that there appears to be a seasonal dependence of the peak and the mean values

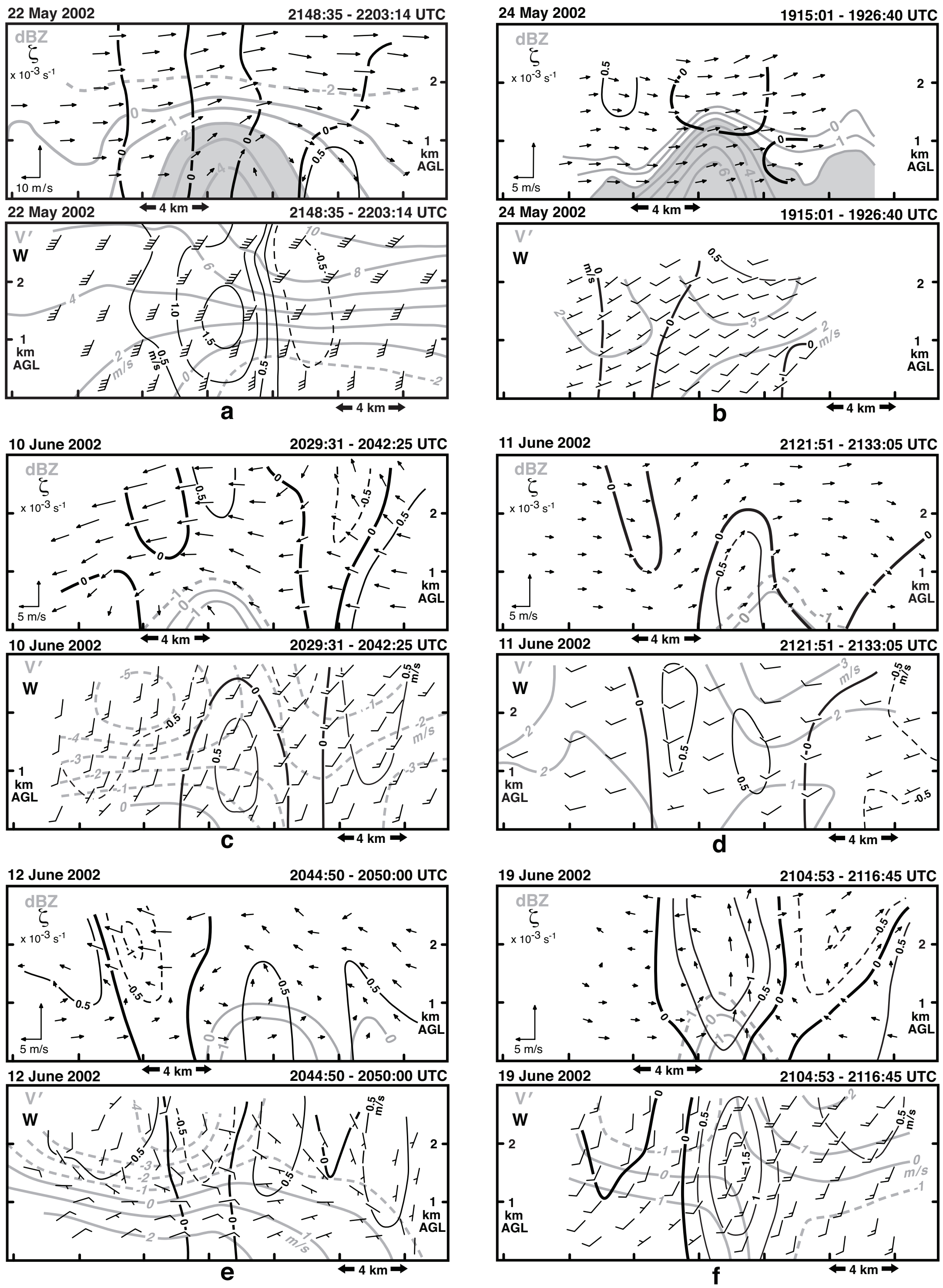

Fig. 3. Mean vertical cross sections perpendicular to the thin line for a) 22 May, b) 24 May, c)10 June, (d) 11 June, (e) 12 June, and (f) 19 June 2002. Top panel: Radar reflectivity (dBZ). Positive (negative) values of vertical vorticity (10^{-3} s^{-1}) are plotted as thin black (dashed) lines. Bottom panel: Positive (negative) values of vertical velocity (m s^{-1}) are plotted as black (dashed) lines. Component of horizontal flow (m s^{-1}) perpendicular to the boundary is plotted. Positive (easterly) and negative (westerly) flow are shown by the gray and dashed gray lines, respectively.

of radar reflectivity. Although there are variations of echo intensity between the six case studies, the echo profiles through the fine lines collected in May are greater than those plotted for the June cases. This would suggest the presence of either smaller and/or fewer scatterers in late spring as a result of insects since this is the primary

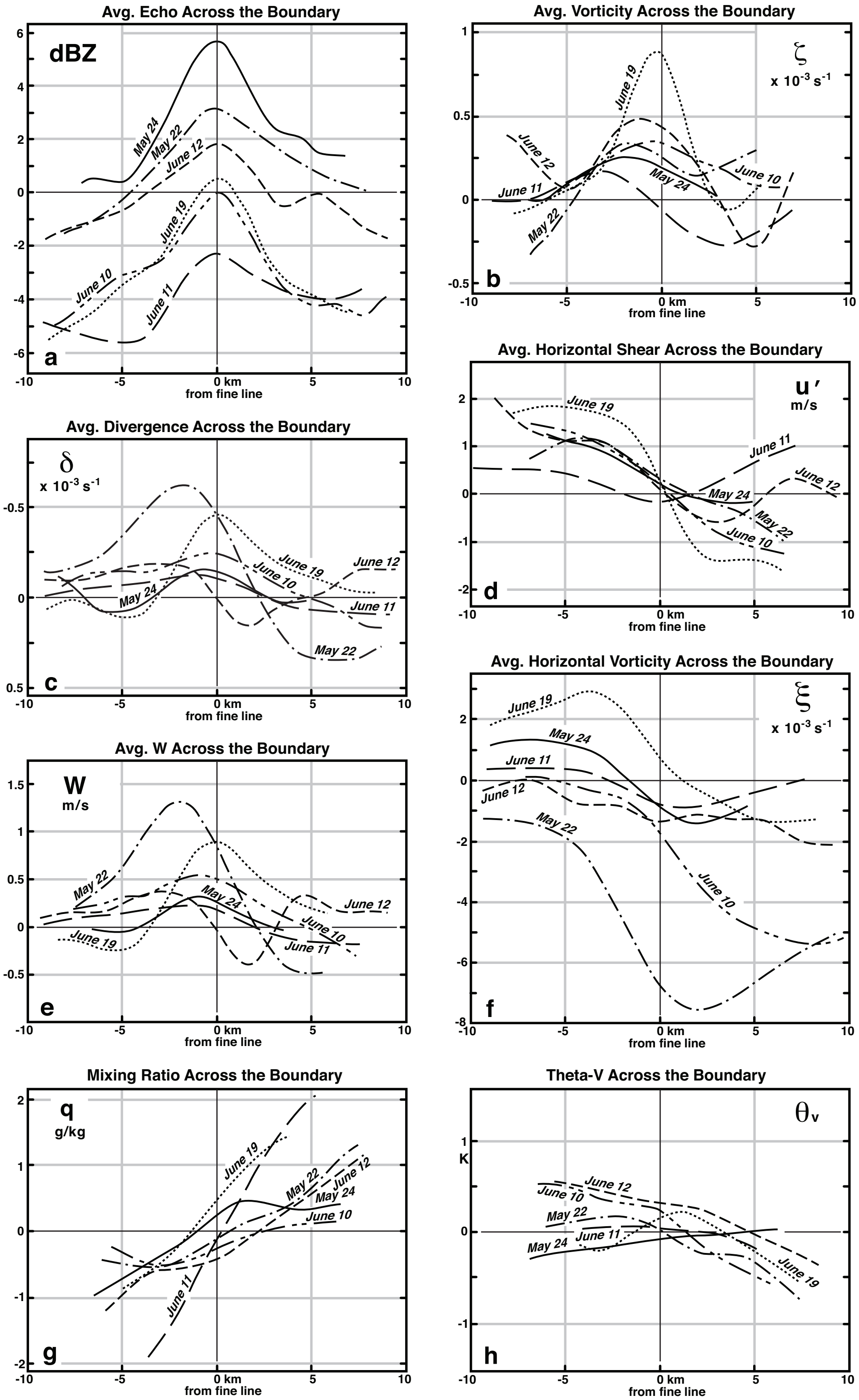

Fig. 4. Profiles across the thin line based on the mean dual-Doppler wind syntheses at 700 m AGL (a-f) or in situ data collected at flight level (g-h). (a) echo intensity, (b) vertical vorticity, (c) horizontal divergence, (d) horizontal shear, (e) vertical velocity, (f) horizontal vorticity, (g) mixing ratio, and (h) virtual potential temperature.

source of echo returns in the clear air (e.g., Geerts and Miao 2005). Note that the echo profiles (except for June 12) are asymmetric with higher background values in the moist versus the dry air masses.

The results from Wilson et al. (1994) suggest that the peak value of radar reflectivity would be associated with the strongest horizontal convergence and updrafts. This may be true for an individual case study but the results shown in Fig. 4a illustrate that this relationship cannot be applied uniformly for different days. The strongest updraft (Figs. 4e) and horizontal convergence (Fig. 4c) occurred on 22 May, however, the increase in echo intensity across the fine line from the dry air mass to the peak value is less than other days (e.g., 24 May) when the updrafts and horizontal convergences were weaker.

The strongest to weakest mean peak updrafts occurred on 22 May and 11 June, respectively (Figs. 4e). These were also the days that experienced the strongest and weakest horizontal convergence (Fig. 4c) highlighting the strong relationship between these two variables. The fine lines were all associated with cyclonic vorticity (Fig. 4b) largely driven by the horizontal shear of the component of the flow parallel to the boundary (u', Fig. 4d). For example, the change of u' across the fine line on 19 June is ~3.25 m s^{-1} over a distance of 5 km (estimated from Fig. 4d) or 6.5 x 10^{-4} s^{-1}. The value is close to the ~8.0 x 10^{-4} s^{-1} maximum value of vertical vorticity estimate from Fig. 4b.

The horizontal vorticity along an axis that is perpendicular to the cross section (Fig. 4f) reveals substantial variability for the 6 cases. The 19 June case, however, is associated with counterrotating horizontal circulations that approximately balance. This situation has been described by Rotunno et al. (1988) as producing updrafts that are vertically erect and, therefore, favorable for the initiation of convection (Fig. 3f). In contrast, the horizontal vorticity pattern accompanying the 22 May convergence boundary (a null case) is dominated by negative values suggesting a strongly tilted updraft over the denser air mass (Fig. 4a).

Average horizontal profiles of mixing ratio and the virtual potential temperature across the boundaries based on in situ measurements collected at flight level are shown in Figs. 4g and 4h, respectively. There is no apparent relationship between the moisture discontinuity and convection initiation. Indeed, the strongest moisture gradient during IHOP was associated with the 11 June null case (Fig. 4g). Moreover, convection initiated on 10 June even though the moisture gradient across the convergence boundary was relatively weak (Fig. 4g). The virtual potential temperature gradients were comparable except for the 24 May and 19 June cases. The former exhibits a reverse temperature gradient even though the moist air mass was denser on a larger scale on this day as depicted by the sounding data. Atkins et al. (1998) also noted that the virtual potential temperature gradient measured within 10 km of a dryline could be different than the larger-scale dryline environment (also noted by Geerts et al. 2006).

5. SOUNDING ANALYSES

An important component of the IHOP data set was the numerous and rapid deployment of dropsondes by the jet flying at midlevels. The flight track was approximately perpendicular to the convergence boundaries. The typical elapsed time to complete the leg was <25 min. An analysis of the frontogenesis (not shown) did not suggest an obvious relationship with convection initiation. An analysis of the solenoidal generation of horizontal vorticity, however, did appear to discriminate between the boundaries that initiated deep convection from the null cases (Fig. 5). The former was characterized by buoyancy gradients that favored the generation of counterrotating horizontal vorticity circulations (24 May, 10 June and 19 June. The latter days (22 May, 11 June, and June 12) were associated with only a single region of horizontal vorticity generation. This result appears to be consistent with the scenario described by Rotunno et al. (1988) suggesting that the generation of horizontal vorticity circulations that produce more erect updrafts are more conducive to convection initiation.

6. SUMMARY AND DISCUSSION

This study represents one of the first comprehensive examinations of convergence boundaries that developed during IHOP. There appeared to be a seasonal dependence of the peak and the mean values of radar reflectivity. Although there are variations of echo intensity between the six case studies, the echo profiles through the fine lines collected in May are greater than those plotted for the June cases. The strongest to weakest mean peak updrafts occurred on 22 May and 11 June, respectively. These were also the days that experienced the strongest and weakest horizontal convergence (Fig. 4c) highlighting the strong relationship between these two variables. It should be noted that no convection developed on 22 May even though the updrafts were, by far, the strongest of all of the 6 cases examined in this study. The fine lines were all associated with cyclonic vorticity largely driven by the horizontal shear of the component of the flow parallel to the boundary.

Average horizontal profiles of mixing ratio and the virtual potential temperature across the boundaries based on in situ measurements collected at flight level were shown. There was no apparent relationship between the moisture discontinuity and convection initiation. Indeed, the strongest moisture gradient during IHOP was associated with the 11 June null case.

Analysis of the horizontal buoyancy gradients derived from a series of soundings across the boundaries suggest that those days when convection developed were associated with the generation of counterrotating horizontal vorticity circulation. These circulations would lead to the development of erect updrafts and increase the likelihood for deep convection.

Acknowledgements. Research results presented in this paper were partially supported by the National Science Foundation under Grant ATM-021048. The National Center for Atmospheric Research is sponsored by the National Science Foundation.

REFERENCE

Atkins, N.T., R.M. Wakimoto, C.L. Ziegler, 1998: Observations of the finescale structure of a dryline during VORTEX 95. *Mon. Wea. Rev.,* **126,** 525-550.

Cai, H., W.-C. Lee, T.M. Weckwerth, C. Flamant, and H.V. Murphey, 2006: Observations of the 11 June dryline during IHOP_2002 – A null case for convection initiation. *Mon. Wea. Rev.*, **134,** 336-354.

Friedrich, K., D.E. Kingsmill, C. Flamant, H.V. Murphey, and R.M. Wakimoto, 2008a: Kinematic and moisture characteristics of a nonprecipitating cold

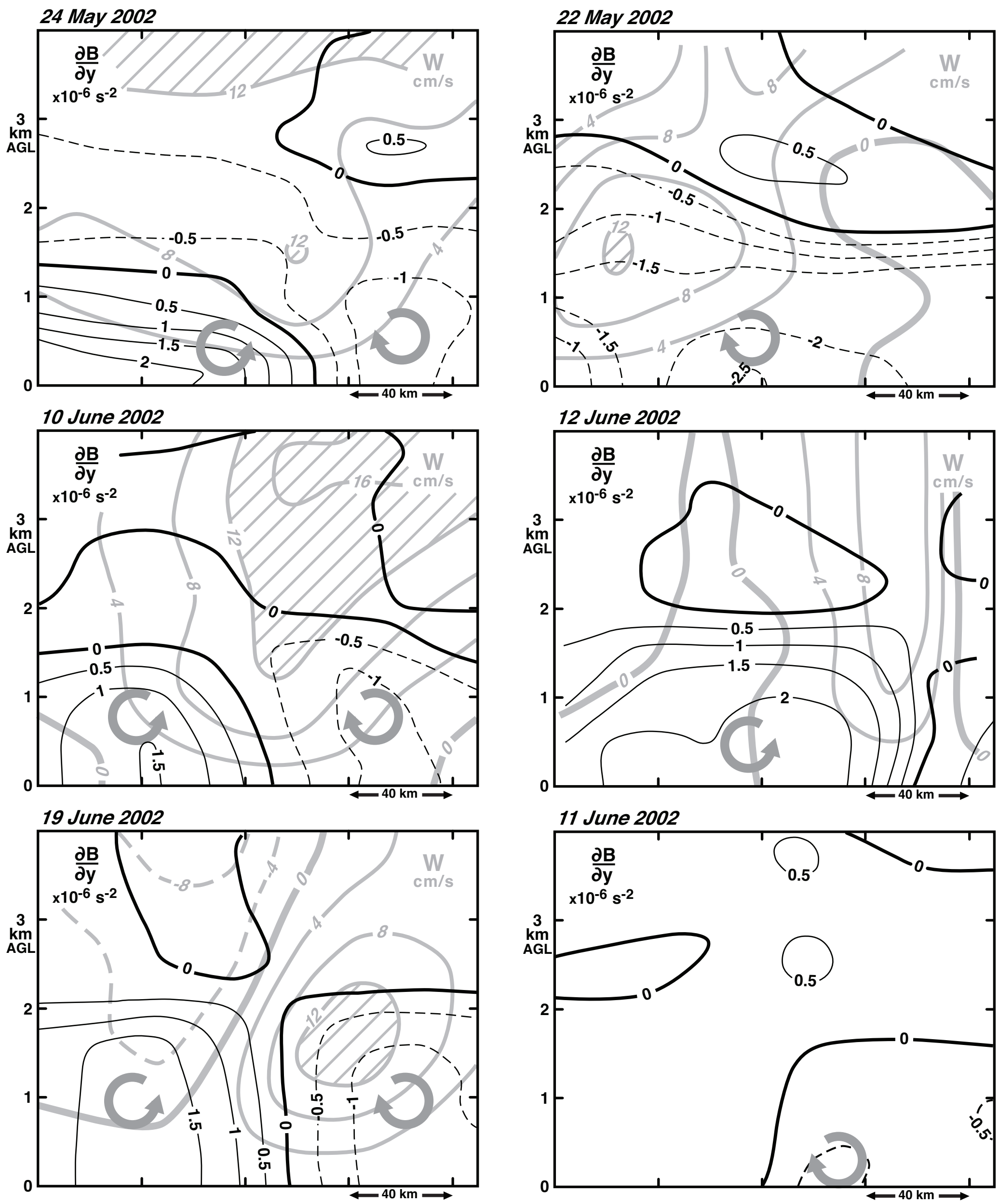

Fig. 5. Vertical cross section through the convergence boundary on 22 May, 24 May, 10 June, 11 June, 12 June, and 19 June. Horizontal gradient of buoyancy (∂β/∂y) perpendicular to the dryline (black lines, 10^{-6} s^{-2}) and vertical velocity (gray lines, cm s^{-1}). The cases are presented such that the days when storms (no storms) developed in the analysis region are plotted on the left-hand (right-hand) side of the figure. Missing wind reports on several soundings prevented an analysis of the vertical velocity field on 11 June.

front observed during IHOP. Part I: Across-front structures. *Mon. Wea. Rev.*, **136,** 147-172.

________, ________, ________, ________, ________, 2008b: Kinematic and moisture characteristics of a nonprecipitating cold front observed during IHOP. Part II: Alongfront structures. *Mon. Wea. Rev.*, **136,** 3796-3821.

Geerts, B., and Q. Miao, 2005: The use of millimeter Doppler radar echoes to estimate vertical air velocities in the fair-weather convective boundary layer. *J. Atmos. Oceanic Technol.*, **22,** 225-246.

________, R. Damiani, and S. Haimov, 2006: Vertical structure of a cold front as revealed by an airborne Doppler radar. *Mon. Wea. Rev.,* **134,** 251-271.

Markowski, P., and C. Hannon, 2006: Observations of convection initiation "failure" from the 12 June 2002 IHOP deployment. *Mon. Wea. Rev.*, **134,** 375-405.

Murphey, H.V., R.M. Wakimoto, C. Flamant, and D.E. Kingsmill, 2006: Dryline on 19 June 2002 during IHOP. Part I: Airborne Doppler and LEANDRE II analyses of the thin line structure and convection initiation. *Mon. Wea. Rev.*, **134,** 406-430

Olsen, D.A., N.W. Junker, and B. Korty, 1995: Evaluation of 33 years of quantitative precipitation forecasting at the NMC. *Wea. Forecasting*, **10,** 498-511.40, 2377-2397.

Purdom, J.F., 1976: Some uses of high-resolution GOES imagery in the mesoscale forecasting of convection and its behavior. *Mon. Wes. Rev.*, **104,** 1474-1483.

_______, 1982 Subjective interpretation of geostationary satellite data for nowcasting. *Nowcasting*, K. Browning, Ed., Academic Press, 149-166.

Richter, H., and L.F. Bosart, 2002: The suppression of deep moist convection near the southern Great Plains dryline. *Mon. Wea. Rev.*, **130,** 1665-1691.

Rotunno, R., J.B. Klemp, and M.L. Weisman, 1988: A theory for strong, long-lived squall lines. *J. Atmos. Sci.*, **45,** 463-485.

Stensrud, D.J., and R.A. Maddox, 1988: Opposing mesoscale circulations: A case study. *Wea. Forecasting*, **3,** 189-204.

Weckwerth, T.M., D.B. Parsons, S.E. Koch, J.A. Moore, M.A. LeMone, B.B. Demoz, C. Flamant, B. Geerts, J. Wang, and W.F. Feltz, 2004: An overview of the International H2O Project (IHOP_2002) and some preliminary highlights. *Bull. Amer. Meteor. Soc.*, **85,** 253-277.

_______, H.V. Murphey, C. Flamant, J. Goldstein, and C.R. Pettet, 2008: An observational study of convection initiation on 12 June 2002 during IHOP_2002. Mon. Wea. Rev., 136, 2283-2304.

Wilson, J.W., and W.E. Schreiber, 1986: Initiation of convective storms at radar observed boundary-layer convergence lines. *Mon. Wea. Rev.*, **114,** 2516-2536.

________, T.M. Weckwerth, J. Vivekanandan, R.M. Wakimoto, and R.W. Russell, 1994: Boundary layer clear-air echoes: Origin of echoes and accuracy of derived winds. *J. Atmos. Oceanic Technol.*, **11,** 1184-1206

_______, N.A. Crook, C.K. Mueller, J. Sun, and M. Dixon, 1998: Nowcasting thunderstorms: A status report. *Bull. Amer. Meteor. Soc.*, **79,** 2079-2099